Model-assisted Identification of the Reaction Mechanism and Kinetics of Cyclohexanone Reduction in a PEM-Cell

Swantje Pauer , Philipp Röse , Yugo Shimizu , Juri Harada , Naoki Shida , Mahito Atobe , Ulrike Krewer

PII: S0013-4686(26)01501-X
DOI: https://doi.org/10.1016/j.electacta.2026.149612
Reference: EA 149612

To appear in: *Electrochimica Acta*

Received date: 2 April 2026
Revised date: 13 July 2026
Accepted date: 26 July 2026

Please cite this article as: Swantje Pauer , Philipp Röse , Yugo Shimizu , Juri Harada , Naoki Shida , Mahito Atobe , Ulrike Krewer , Model-assisted Identification of the Reaction Mechanism and Kinetics of Cyclohexanone Reduction in a PEM-Cell, *Electrochimica Acta* (2026), doi: https://doi.org/10.1016/j.electacta.2026.149612

Highlights

- Experimentally validated kinetic model identifies the reaction mechanism for ketone reduction
- Ketone adsorption and alcohol desorption identified as key kinetic limitations.
- Slow alcohol desorption and competitive HER govern efficiency at higher current densities.
- Simulations predict improved Faradaic efficiency with increased surface area or ketone concentration.

Model-assisted Identification of the Reaction Mechanism and Kinetics of Cyclohexanone Reduction in a PEM-Cell

Swantje Pauer [a], Philipp Röse [a], Yugo Shimizu [b], Juri Harada [b], Naoki Shida [b], Mahito Atobe [b], and Ulrike Krewer *[a]

a *Institute for Applied Materials – Electrochemical Technologies*
Karlsruhe Institute of Technology
Adenauerring 20b, 76131 Karlsruhe, German)
E-mail: ulrike.krewer@kit.edu

b *Department of Chemistry and Life Science*
Yokohama National University
Yokohama 240-8501, Japan.

Abstract:

The kinetics of electroorganic synthesis reactions is usually not analyzed, which prevents knowledge-driven design and operation. This study examines the electrochemical *cis*-selective reduction of 4-*tert*-butylcyclohexanone to 4-*tert*-butylcyclohexanol using an Rh/C catalyst in a proton exchange membrane (PEM) cell. The reaction mechanism and kinetics are identified using a combination of experimental cyclic voltammetry (CV) and model-based kinetic analysis. Among three proposed reaction mechanisms – one based on Langmuir-Hinshelwood and two based on Eley-Rideal theory – the Langmuir-Hinshelwood-type mechanism (LHM), involving the reaction of adsorbed 4-*tert*-butylcyclohexanone with adsorbed hydrogen, was identified as the most plausible. Dynamic simulations based on the LHM showed strong agreement with the experimental data, accurately capturing key electrochemical features and reproducing Faradaic efficiencies. The kinetic model accounts for reaction kinetics for the electroreduction and the competitive hydrogen evolution reaction, as well as mass transport processes. Our findings highlight that ketone adsorption influences both catalytic activity and selectivity, whereas alcohol desorption is identified as the rate-limiting step. The accumulation of alcohol at the catalyst surface reduces active site availability and promotes H_2 evolution, thereby lowering Faradaic efficiency at higher current densities. Simulations under steady-state conditions predict that increasing

ketone concentrations reduces side reactions and increase the Faraday efficiency for the desired product. These insights emphasize the importance of optimizing catalyst properties to enhance overall conversion rate, and of maintaining high ketone concentration to achieve high selectivity, energy efficiency, and Faradaic efficiency. Kinetic analysis is thus shown to be a powerful prerequisite for understanding and improving synthesis processes.

Keywords: electrosynthesis, electrochemical reaction kinetics, reaction mechanism, kinetic modeling, process optimization

1. Introduction

Organic electrochemistry is a potential enabler for the electrification of the chemical industry and its transition to more sustainable processes: by using renewable electricity as a reactant, it offers a sustainable alternative to traditional synthesis methods that often rely on hazardous and toxic chemicals.[1–3]

The diastereoselective electrochemical reduction of cyclic ketones to alcohols is of particular interest as the resulting products are essential building blocks in the synthesis of fragrances and pharmaceuticals.[4–6] An important example is 4-*tert*-butylcyclohexanol **2a**, which is produced at annual scales, exceeding 1,000 tons, and is widely utilized in cosmetics, soaps, and various domestic products.

The *cis*-isomer is more valuable than the *trans*-isomer, due to its better aromatic characteristics. Thus, a diastereoselective synthesis method is required.[7] Many homogeneous and heterogeneous synthesis methods using a catalyst and H_2 gas face challenges in achieving high yields and selectivity.[8–10]

While homogeneous catalysts can offer excellent intrinsic activity and selectivity, heterogeneous electrocatalysts are attractive for practical, scalable operation and straightforward product separation.

Several electrosynthesis methods have been explored for the reduction of cyclic ketones to alcohols: the 1,4-reduction of α,β-unsaturated ketones using ammonium chloride,[11] the reductive cyclization of non-conjugated acetylenic ketones to 2-methylenecyclopentanols,[12] the deoxygenative reduction of ketones using paired electrolysis,[13] cerium- and nickel-mediated synthesis methods,[14] as well as stereoselective approaches.[15]

Recently, Atobe and co-workers reported the diastereoselective electrochemical reduction of cyclohexanones on various noble metal catalysts in a Proton Exchange Membrane (PEM) cell (Fig. 1)[16].

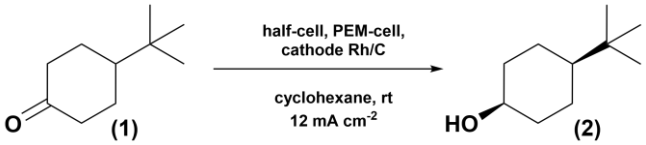

Fig. 1. Electrocatalytic hydrogenation of 4-*tert*-butylcyclohexanone (1a) to *cis*- and *trans*-4-*tert*-butylcyclohexanol (2a) on Rh/C.[16]

Using Rh on carbon support and cyclohexane as solvent, 4-*tert*-butylcyclohexanone **1a** was reduced in the presence of protons to 4-*tert*-butylcyclohexanol **2a** with up to 94% *cis*-selectivity and 93% current efficiency.

Water oxidation was employed as the anodic counter-reaction, supplying the required protons through the Nafion membrane to the cathode. Besides the desired alcohol, H_2 is produced as a byproduct.

This approach is highly efficient and sustainable, enabling gram-scale production of high-value *cis*-4-*tert*-butylcyclohexanol **2a** (5 g in 76 h) via continuous circular flow in a single PEM cell, consuming only electrical energy, **1a**, and water, without the need for H_2 gas. Further, their setup operates under mild conditions, ambient temperature and pressure, and does not require a supporting electrolyte.[17–24] While this method uniquely combines high *cis*-selectivity, sustainability, and operational simplicity, the current densities reported (12-36 mA cm^{-2}) are modest compared with those of conventional PEM water-electrolysis systems, which routinely operate above 1 A cm^{-2}.[25,26] This highlights the need to further optimize catalytic activity and surface interactions to fully realize the potential of this concept for scalable applications. However, the exact reaction mechanism, kinetics, and their resulting limitations are still unclear. Understanding all reactions quantitatively, as well as the interactions between reactions and mass transport, is essential for targeted optimization of synthesis, cell, and operating conditions in terms of conversion rate, selectivity, and energy efficiency. In their previous study, Shimizu et al. have emphasized the role of adsorption geometry in determining diastereoselectivity, suggesting that surface interactions play a decisive role in product distribution, while the kinetic implications of surface interactions remain largely unexplored.[16] Questions remain about the specific pathways and intermediates involved, highlighting the need for a kinetic analysis that systematically and quantitatively investigates the role of surface processes and operating conditions on the overall performance of the reaction. Mechanistic frameworks such as Langmuir-Hinshelwood and Eley-Rideal offer a physically consistent basis for analysing surface reactions, incorporating adsorption, surface coverage, and the nature of reactive encounters.[27] Previous studies have demonstrated that distinguishing between these

mechanisms is not only conceptually important but also experimentally and computationally feasible, and remains an actively pursued objective in surface heterogeneous kinetics.[28,29]

Dynamic kinetic modeling and simulation is an efficient tool for evaluating and discriminating between different reaction pathways and kinetics, and the impact of transport processes.[30–32] Once a suitable model is established, electrochemical measurements, like cyclic voltammograms (CVs), can be interpreted more quantitatively and can be used as a diagnostic tool to guide further optimization.[33–36] Despite their potential, such modeling approaches have rarely been applied to electro-organic synthesis. Simulations of large organic molecules remain scarce, with only a few studies employing molecular simulations, computational fluid dynamics, or potential-dependent kinetic models. A recent review by Röse et al. provides an overview of the available modeling strategies.[3]

This study introduces the first dynamic kinetic model for the electrochemical reduction of 4-*tert*-butylcyclohexanone **1a** in a PEM cell. By combining the analysis of experimental CVs and dynamic kinetic modeling and simulations, we identify the most plausible reaction pathway and the role of adsorption, species interaction, transport, and potential. In addition, we demonstrate that the model can be applied to steady-state simulations and used to forecast how changes in operating parameters influence current efficiency and product selectivity under practical conditions. This work advances mechanistic insight and furnishes a predictive platform for the rational optimization of electrochemical ketone reductions.

2. Methodology

This section outlines experimental methods, mechanistic assumptions, and the applied kinetic model.

2.1. Materials and Equipment

Reagents and solvents were purchased from commercial sources and were used without further purification. Nafion® 117 membrane was purchased from Furukawa Agency and Nafion® DE521 ionomer was purchased from Sigma-Aldrich. Fuel cell catalysts TEC10E50E; Pt/Ketjenblack

(Pt/C; 46.1 wt.%) and TECRh(ONLY)E30; Rh/Ketjenblack (Rh/C; 28.9 wt.%), were purchased from Tanaka Kikinzoku Kogyo. Carbon paper (Sigracet® GDL39BB, PTFE/carbon fiber backbone with microporous layer (MPL)) was purchased from SGL CARBON. Electrolysis under single-flow operation was performed with a syringe pump (KDS100, KD Scientific). Cyclic voltammetry and electrochemical impedance spectroscopy were performed on an electrochemical analyzer (ALS/CH Instruments 660E, BAS). Scanning electron microscopy (SEM) measurements were carried out with a VE-8800 microscope (KEYENCE) operated at 10 kV.

2.2. Membrane Electrode and Cell Assembly

Pt/C was used as anode catalyst material, and Rh/C was used as cathode catalyst material. Catalyst inks were prepared by mixing the catalyst with deionized water, ionomer, and 1-propanol. The ionomer-to-carbon support mass ratio was 4:5. The microporous layer of the carbon paper was coated with the catalyst ink using a stainless-steel mask (1 cm x 4 cm). The catalyst loading of each metal catalyst was 0.5 mg cm-2 for anode and cathode. Afterward, the coating was dried for 10 min at 60 °C and then hot-pressed (0.4 MPa, 120 °C) for 1 min. The membrane electrode assembly (MEA) was done by placing the membrane (3.5 cm x 10 cm) between the coated anode and cathode carbon paper sheets with the catalyst-coated sides towards the membrane, and the assembly was hot-pressed (0.4 MPa, 120 °C) for 1 min. The cross-sectional SEM image of the coated carbon paper anode (Fig. 2A) was taken before hot-pressing the MEA and shows a catalyst layer thickness of 40 μm over the MPL (55 μm) and the PTFE/carbon fiber backbone (294 μm).

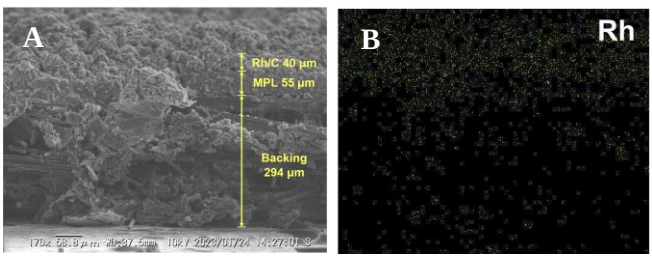

Fig. 2. SEM Image (A) of the anode with catalyst layer, MPL and carbon fiber backing prior to hot pressing. The elemental mapping (B) shows the distribution of Rh catalyst throughout the layers.

Based on these layer thicknesses and the manufacturer-provided compression behavior under the applied assembly conditions the post-pressing layer thicknesses were approximated for modeling (Table S2).

The element mapping indicates that most of the Rh catalyst is located above the MPL, with only a few particles inside the porous electrode (Fig. 2B).

The PEM cell was assembled by placing the MEA in between Teflon® gaskets, carbon separators, and gold-plated stainless-steel plates on each side and tightened with screws (M6) to 3.0 Nm using a torque wrench. The cathode end plate was connected to a syringe pump for supplying 4-*tert*-butylcyclohexanone **1a** in cyclohexane. The anode end plate was attached to a mass flow controller supplying the anode constantly with humidified H2/N2 (20:80 vol%). The anode configuration (Pt + H2|2H+) serves as dynamic hydrogen reference electrode (DHE). [16,37] Due to the fast hydrogen oxidation reaction (HOR) kinetics on Pt and the low current densities employed (< 30 mA cm^{-2}), the DHE potential was assumed to remain close to the equilibrium H_2/H^+ potential throughout the experiments; further, both electrodes see the same electrolyte concentration. Consequently, all electrode potentials discussed in this work are reported on the RHE scale.

2.3. Electrochemical Measurements

Cyclic voltammetry (CV) was performed using the Rh/C coated cathode as working electrode and the Pt/C coated anode as the DHE (corresponding to the RHE scale). At the cathode, 4-*tert*-butylcyclohexane in cyclohexane (0 M, 0.01 M, 0.05 M, 1M) was supplied by a syringe pump with a flow rate of 4 mL h^{-1}, whereas humidified H_2 (100 vol%) was provided to the anode with a flow rate of 50 mL min^{-1}. The cell temperature was set to room temperature. Cyclic voltammograms were measured in the potential range from −0.15 to 0.4 V vs. RHE at scan rates of 10, 5, and 1 mV s^{-1}. Electrochemical impedance spectroscopy was performed at −0.1 V vs. RHE from 100 kHz to 0.1 Hz using an amplitude of 0.5 mV. Membrane resistances were determined before each experimental series by supplying humidified H_2 (100 vol%) to

anode and cathode for 1 h and measuring the ionic resistance by EIS. The ohmic resistance, attributed mainly to the membrane due to negligible electric losses and thin electrode layers compared to the membrane, was taken from the high-frequency intercept of the Nyquist plot for iR-correction.

2.4. Reaction Mechanisms

2.4.1. Proposed Mechanisms

Only H_2 and *cis*- and *trans*-isomers of 4-*tert*-butylcyclohexanol **2a** ($C_{10}H_{20}O$, subsequently referred to as alcohol) were found as products, suggesting HER and the conversion of 4-*tert*-butylcyclohexanone **1a** ($C_{10}H_{18}O$, subsequently referred to as ketone) to alcohol as reactions, as cyclohexane (C_6H_{12}) does not react.[16] As the surface is known to play a role in the kinetics, we evaluate whether the ketone or proton, or both, need to be adsorbed for the alcohol production.[16] Furthermore, C_6H_{12} adsorption on Rh is assumed to be negligible.[16] This is further supported by Garcia-Pintos et al., who report weak adsorption energies for C_6H_{12} on Rh.[38] We propose three possible reaction mechanisms for the electrochemical reduction of ketone to alcohol based on the theories of Langmuir-Hinshelwood (LHM) and Eley-Rideal (ERM1 and ERM2, Fig. 3).[27] The mechanisms assume different adsorption behavior of the substrates on the Rh catalyst surface. The Langmuir-Hinshelwood Mechanism assumes the adsorption of both reactants, ketone and protons, at the catalyst surface. Protons get electrochemically reduced to adsorbed hydrogen atoms in a Volmer-step. In a surface-controlled reaction sequence, hydrogen atoms and ketone react to adsorbed alcohol, which then desorbs from the surface. Additionally, the adsorbed hydrogen (*H) can react to H_2 and desorb in a Tafel step. The two Eley-Rideal mechanisms (ERM 1 and 2) assume that only one of the reactants adsorbs on the Rh surface, whereas the other one reacts from the solution or the ionomer with the adsorbed intermediate. In ERM1, only protons adsorb electrochemically in a Volmer-step to hydrogen atoms, which react with the dissolved ketone in a purely chemical step to form adsorbed alcohol. In ERM2, only the ketone is adsorbed and reacts in two successive proton-coupled electron transfer steps with an adsorbed radical as

intermediate to form the product. The desorption of the radical is not considered, as it was not detected experimentally in solution.[16] The introduction of the intermediate is based on the methodological decision to decompose the mechanism into elementary steps. Further, transfer of two electrons in a single step is highly unlikely for electrochemical reactions.[39] Both ERM1 and ERM2 consider the desorption of the alcohol and the replenishment of the free surface site (*= Rh/C). Since H_2 is experimentally detectable[16] and Rh sits near the top of the HER volcano plot due to its near-optimal hydrogen adsorption energy[40], we assume that the hydrogen evolution reaction (HER) takes place as a competing reaction. The associated H_2 formation and the electrochemical H^+ reduction are included in the schemes in Figure 3. The full reaction equations are given in the supportive information in Tab. S4-6.

2.4.2. Mechanism and Kinetics Identification

The here applied scenario-based model identification is based on previously published approaches for oxygen evolution by Geppert et al.[31] and sulfur reduction by Schön et al.[41]. Dynamic kinetic simulations in combination with experimental CVs are used to differentiate the proposed reaction mechanisms and to identify the most feasible one.

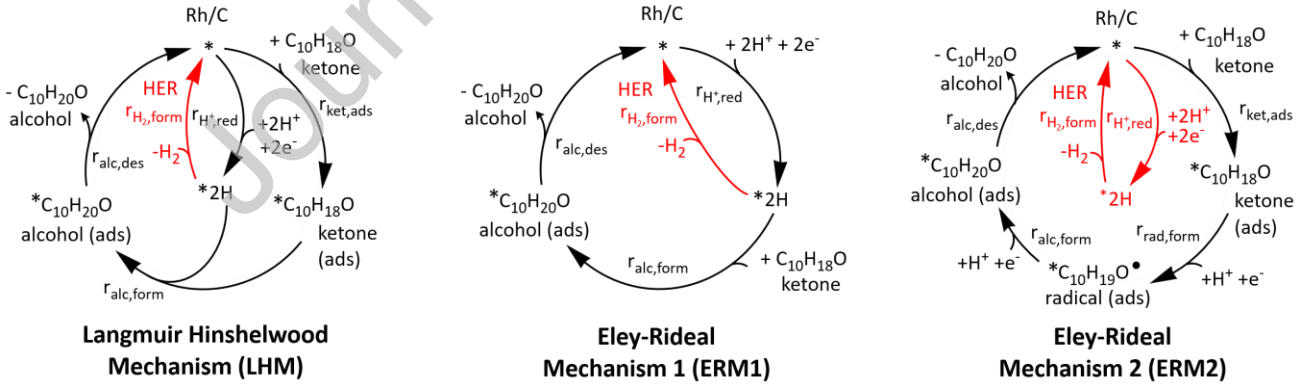

Fig. 3. Proposed reaction mechanisms for the electrochemical reduction of 4-*tert*-butylcyclohexanone **1a** (ketone) to 4-*tert*-butylcyclohexanol **2a** (alcohol): A) Langmuir Hinshelwood mechanism, B) Eley-Rideal mechanism 1 (only adsorbed hydrogen considered), and C) Eley-Rideal mechanism 2 (only adsorbed ketone considered). All mechanisms assume the hydrogen evolution reaction (HER) as a competing side reaction.

The approach includes the agreement of the simulation to experimental data under different operating conditions and an analysis of the reaction rates, surface coverages, and thermodynamic parameters. We consider different scan rates, and reactant concentrations. Furthermore, our approach includes the agreement of faradaic efficiencies from quasi-steady state simulations with experimental faradaic efficiencies from constant current electrolysis.[16] The agreement of the mechanistic assumptions and simulation with the experimental data is taken as a measure of the feasibility of the proposed mechanisms and their corresponding kinetics.

2.5. Kinetic Model

2.5.1. Model Overview

The dynamic kinetic model describes the above-mentioned reactions at the cathode and the mass transport of ketone, alcohol, and H_2 through the diffusion layer, which consists of an outer PTFE/carbon fiber backing and an inner microporous layer (MPL) between the electrode and the bulk, i.e., transport channel (Fig. 4). Protons enter from the opposite direction from the anode through the membrane, via migration. Hydrogen oxidation at the anode is considered to be fast and have negligible overpotential, in effect acting as a dynamic hydrogen electrode. The electrochemical reactions are simulated using Butler-Volmer kinetics. Surface species are balanced at the electrode through dynamic species and charge balances, treating reactions as sources or sinks. The proposed reaction mechanisms define the characteristics and amount of the adsorbed surface species, reactions involved in the process, and the reaction rates.

The model is 1D-discretized from the catalyst layer (x=0) through the diffusion layer to the bulk to simulate ketone, alcohol and dissolved H_2 transport and concentration profiles. The bulk phase includes the ketone at constant concentration due to continuous, over-stoichiometric supply, and the products, alcohol and H_2, at zero concentration, as they are removed with the flow. The solvent cyclohexane (C_6H_{12}) is shown in Fig. 4 for completeness but is not included in the model equations, as it can be assumed that it does not participate in the reaction.[16] Backing layer and MPL consist of several volume elements of uniform thickness $\Delta x_{Backing}$ and Δx_{MPL}, with thicknesses determined by the number of elements and layer

thickness, respectively (Table S2). $x = \delta_{mpl}$ represents the interface between the two diffusion layers, where concentrations are equated via a Dirichlet boundary condition at the interface. $x = \delta_{total}$ represents the boundary of the backing to the bulk solution. Proton transport through the ionomer and membrane is migration only, with a fixed concentration; thus, the impact of the membrane is included as a resistance term. The electrode is not discretized and is modeled as a planar interface between the diffusion layer and the membrane. As the catalyst layer is thin compared to the diffusion layer, concentration gradients are assumed to be negligible.[42] The first volume element of the MPL at the boundary to the electrode is the reaction plane, in which reaction and diffusion flux are considered.

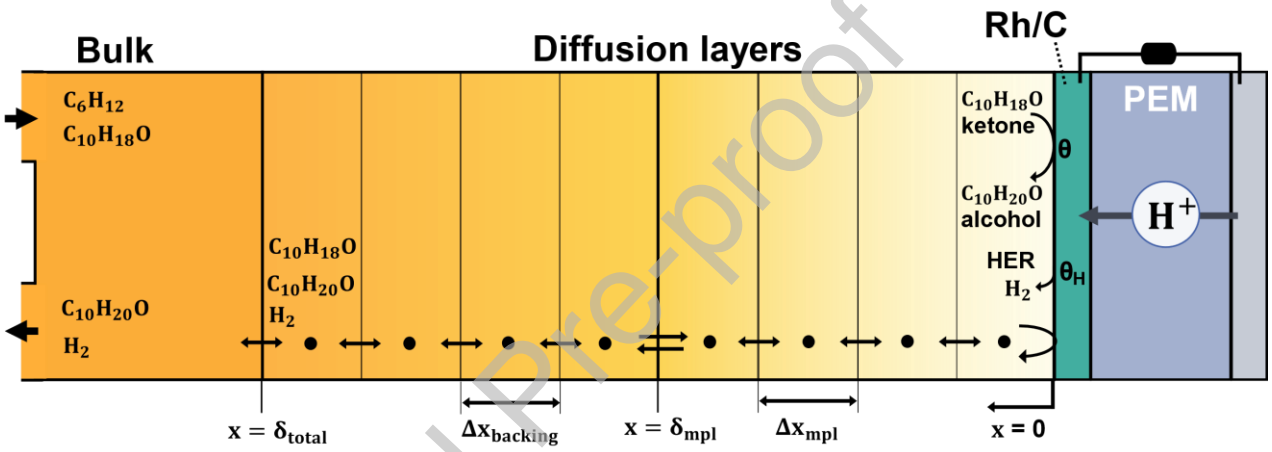

Fig. 4. Scheme of the reaction kinetic model of the ketone reduction, including the reactions at the Rh/C electrode, the 1-D diffusive transport of reactants and products through the diffusion layer towards and away from the catalyst layer at the cathode, and proton migration through the membrane.

2.5.2. Reaction Rate Equations

The surface specific rates $\mathbf{r_i}$ of each surface reactions, adsorption, and desorption i are calculated by the following equations. The rate equations of the electrochemical reactions based on Butler-Volmer contain a cathodic (eq. (1)) and anodic (eq. (2)) term, with each having an exponential dependence on electrode potential E, a kinetic constant k and a dependence on activity of the reactants in the solution, a_j and surface coverages θ by adsorbate j, the charge transfer coefficient α_i for

one-electron transfer reaction steps, Faraday constant F, and RT, the product of the universal gas constant and temperature. ν_{ij} is the stoichiometric factor of species j in reaction i.

$$r_i = k_{+i} \cdot \prod_j \left(a_j^{\nu_{-ij}} \cdot \theta_j^{\nu_{-ij}}\right) \cdot \exp\left(\frac{-(1-\alpha_i)FE}{RT}\right) \quad (1)$$

$$-k_{-i} \cdot \prod_j \left(a_j^{\nu_{+ij}} \cdot \theta_j^{\nu_{+ij}}\right) \cdot \exp\left(\frac{\alpha_i FE}{RT}\right) \quad (2)$$

Contributions from open circuit potential E^0 are included in the rate constants. The activities a of all species in the solution are calculated as the ratio of concentration divided by the standard concentration of 1 mol L^{-1}, assuming activity coefficients of 1. Chemical surface reactions and sorption processes (adsorption and desorption) are described similarly, but without explicit potential dependence (eq. (3) and (4)).

$$r_i = k_{+i} \cdot \prod_j \left(a_j^{\nu_{-ij}} \cdot \theta_j^{\nu_{-ij}}\right) - k_{-i} \cdot \prod_j \left(a_j^{\nu_{+ij}} \cdot \theta_j^{\nu_{+ij}}\right) \quad (3)$$

$$r_{ads,j} = k_{ads} \cdot a_j \cdot \theta_*, \quad r_{des,j} = \cdot k_{des} \cdot \theta_j \quad (4)$$

Adsorption steps explicitly account for the availability of free surface sites θ_* through the site-balance condition (eq. (5)).

$$\theta_* = 1 - \sum_j \theta_j \quad (5)$$

The full set of equations is provided in the supporting information (section S2.3).

2.5.3. Balance of Species

The reactions at the electrode lead to a concentration gradient in the diffusion layer, which in turn causes a diffusive flux of species j in the solution, as described by eq. 6:

$$\frac{\partial c_{j,n}}{\partial t} = D_{eff,j} \frac{\partial^2 c_{j,n}(x,t)}{\partial x^2} \quad (6)$$

The diffusion coefficients $D_{eff,j}$ are calculated using the method introduced by Tyn and Calus et al.[43] and the group contribution method (eq. (7)). Here, V_j and V_{C6H12} are the molar volumes of the species j

and the solvent C_6H_{12}, and P_j and P_{C6H12} the parachors. The values, including the kinematic viscosity μ_{C6H12} are given for ambient Temperature T in Table S2.

$$D_{eff,j} = \frac{\varepsilon}{\tau} \cdot 8.93 * 10^{-8} \cdot \left(\frac{V_j^{\frac{1}{6}}}{V_{C_6H_{12}}^{\frac{1}{3}}} \right) \left(\frac{P_{C_6H_{12}}}{P_j} \right)^{0.6} \frac{T}{\mu_{C_6H_{12}}} \quad (7)$$

MPL and backing layer have different porosities ε (Table S2), resulting in different effective diffusion coefficients. Tortuosity τ in the GDL and MPL is negligible due to their high porosity (Table S2).[44,45]

Changes in the coverage of species on the electrode surface are modelled using a species balance (eq. (8)) that includes the areal concentration of adsorption sites Γ and the geometric electrode area A:[33]

$$\frac{\mathrm{d}\theta_j}{\mathrm{dt}} = \frac{1}{\mathrm{A} \cdot \Gamma} \sum_i \nu_{ij} \cdot (\mathrm{r}_{+i} - \mathrm{r}_{-i}) \quad (8)$$

2.5.4. Charge Balance

The charge at the electrode's surface is balanced by considering the accumulation of charge q, with the electrode potential at the electrode-liquid interface E, and the double layer capacitance C_{dl}, due to charge transport, i. e. total current density j and the faradaic current density j_F caused by reactions:

$$\frac{dq}{dt} = C_{dl} \frac{dE}{dt} = j - j_F \quad (9)$$

The total current is calculated using Ohm's law with the potential drop due to the internal resistance R_u determined by electrochemical impedance spectroscopy and the geometrical area A (eq. (10)). The externally applied potential is referred to by E_{ext}. Faraday's law is used to calculate the faradaic current density from the reactions (eq. (11)).

$$j = \frac{E_{ext} - E}{R_u \cdot A} \quad (10)$$

$$j_F = F \cdot \sum_i z_i \cdot r_i \quad (11)$$

The model is formulated to simulate CV experiments. The externally applied potential E_{ext} changes linearly over time between an upper and lower potential at a defined scan rate v according to equation eq. 12.

$$E_{ext}(t) = \begin{cases} E_{ext}(t=0) - vt, & \forall\, t < t_s \\ E_{ext}(t=t_s) + vt, & \forall\, t \geq t_s \end{cases} \quad (12)$$

The potential is initially scanned from a high to a low potential. Upon reaching the potential minimum at the switching time $\mathbf{t_s}$, the scan direction reverses, marking the end of the cathodic scan (negative direction) and the start of the anodic scan (positive direction).

The model is implemented in MATLAB 2023b and uses the **ode15** solver function for differential equations. To ensure high accuracy, settings include an absolute error tolerance of 10^{-15} and a maximum step size of 0.1 seconds.

2.5.5. Experimental Parametrization.

The experimental CV data for different scan rates is used to determine the areal double-layer capacitance C_{dl} as described in detail in the supporting information (SI) in section S1.1. The kinetic parameters k_{+i}, k_{-i}, α_i, and Γ were identified by experimental parametrization, using CV experiments and mathematical parameter optimization. The number of kinetic parameters depends on the assumed reaction mechanism. The built-in MATLAB functions particle-swarm and pattern-search were used to identify the parameters by optimization to minimize the root mean squared error (RMSE) between experimental and simulated current densities (eq. 13). Here, N represents the number of data points (N = 1100 per cycle), where j_{sim} and j_{exp} denote the simulated and experimental current density values, respectively, recorded at each data point during the third CV cycle.

$$RMSE=\sqrt{\frac{\sum_{n=1}^{N}\left(j_{sim}-j_{exp}\right)^2}{N}} \quad (13)$$

Parameter optimization was performed at a ketone concentration of 1 M and a scan rate of 10 mV s^{-1} using experimental CVs. For validation, CVs at various scan rates and ketone concentrations with lower values were used.

3. Results and Discussion

In the following, we will first qualitatively analyze the experimental data to extract information on the mechanism, then the remaining mechanisms are evaluated in terms of the ability of the respective models to reproduce the experimental data, followed by an in-depth analysis of the reaction and transport interaction and limitations.

3.1. Analysis of Experimental Data

Cyclic voltammograms were recorded as described in section 2.3 under a range of operating conditions to evaluate the dependence of the CV on potential, transport, and concentration. Figure 5 shows the results for the 3rd cycle of the CV measurements at scan rates of 10, 5, and 1 mV s^{-1} for a ketone concentration *c* of 1 M and for 10 mV s^{-1} at ketone concentrations of 0.05, 0.01, and 0 M. The CVs are iR-corrected with the corresponding resistance $R_{u,c}$ (Table S2).

Fig. 5A displays for 1 M ketone concentration and 10 mV s^{-1} a smooth cathodic reduction curve with no significant slope changes, indicating the absence of clearly separable multi-step processes. Two broad and indistinct peaks in the anodic scan at –0.02 V and 0.14 V vs. RHE suggest partial reversibility of at least one electrochemical reaction. Fig. 5B shows a similar trend for 5 mV s^{-1} with slightly lower cathodic current density (-19.97 mA cm^{-2}) and reduced anodic response. In contrast, at 1 mV s^{-1} (Fig. 5C) the CV resembles a polarization curve with minimal hysteresis. The onset of the cathodic current is shifted by –0.1 V to lower potentials, and the anodic peaks shift to -0.0052 V and 0.147 V. A distinct cathodic peak

at -0.0049 V, absent at higher scan rates, may indicate the reduction of a transient intermediate accessible only under slow scan conditions. With increasing scan rate, the onset potential shifts positively, hysteresis grows, and anodic currents rise, indicating increasing kinetic constraints and partial reversibility of at least one intermediate.

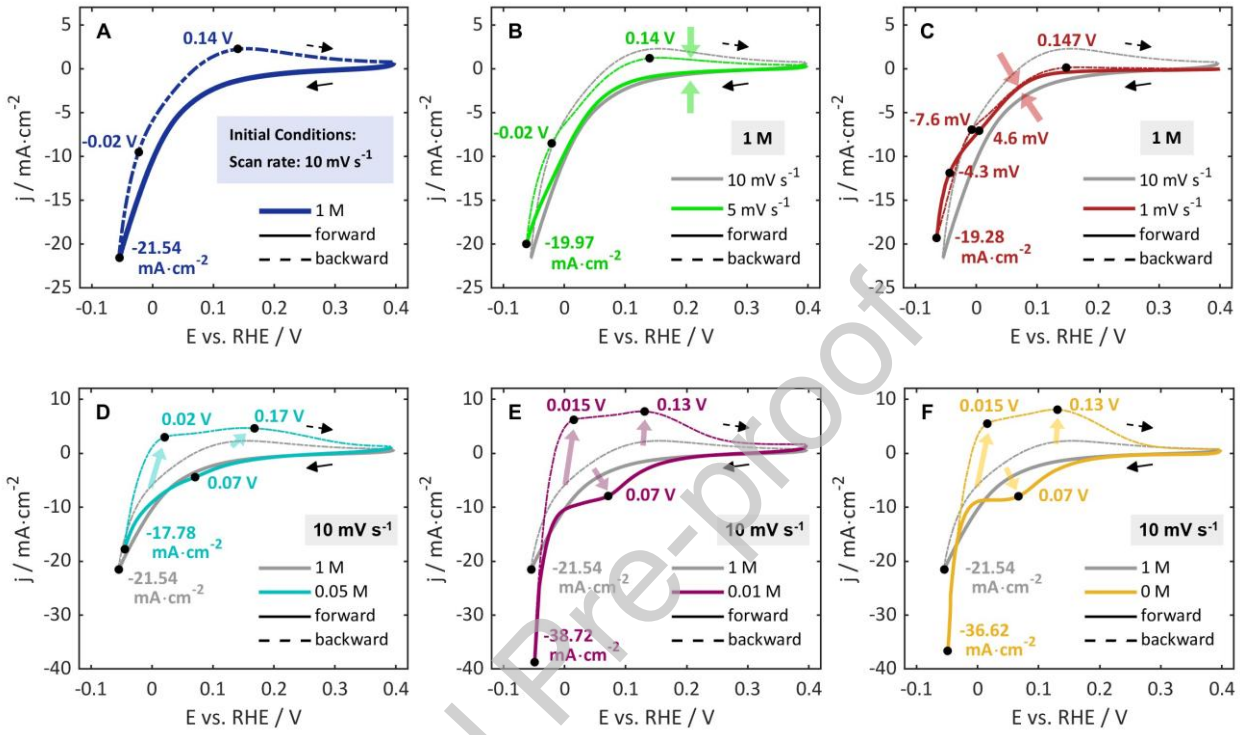

Fig. 5. Impact of scan rate and concentration on iR-corrected experimental CVs: A) 1 M ketone concentration at a scan rate of 10 mV s^{-1}, B) comparison to 5 mV s^{-1}, and C): 1 mV s^{-1}. Comparison at 10 mV s^{-1} for 0.05 M (D), 0.01 M (E), and 0 M (F) ketone concentration. For brevity, the negative-going and positive-going scans are denoted as forward and backward, respectively.

While the variations in scan rate reveal some kinetic influences and partial reversibility, the overall differences remain subtle and do not allow for a conclusive mechanistic interpretation.

By analyzing the changes in the features in the CVs with concentration variations, we can obtain further information on the kinetics and reaction mechanism of the concentration dependence of ketone reduction and its interaction with hydrogen evolution as the side reaction. Therefore, we investigated ketone reduction with strongly reduced ketone concentrations of 0.05 M, 0.01 M, and no ketone at a scan rate of 10 mV s^{-1} (Fig. 5D-F). The case of 0 M ketone allows to study pure hydrogen evolution, whereas small

concentrations of ketones allow to show the interaction of HER with ketone species and a possible blocking of sites. To directly visualize the concentration-dependent changes in the voltammetric response, each concentration is compared individually to the CV at 1 M ketone concentration. The resulting differences provide insight into the interaction between ketone reduction and HER.

At a ketone concentration of 0.05 M (Fig. 5D), a redox peak occurs at 0.07 V in the negative going scan, which was not observed at higher concentrations, and two peaks during the positive going scan at 0.02 V and 0.17 V versus RHE. The changes indicate a change in the prevalence of reaction processes on the surface. Most likely, in this case, the impact of ketone redox processes decreases, while that of hydrogen redox processes increases, compared to the CV at 1 M ketone concentration. The same redox characteristics are found for 0.01 M and without ketone concentration; the corresponding current densities are higher, and the shape of the features is more pronounced (5E and F). The oxidation peak at 0.13 V corresponds clearly to that observed at high concentrations; the oxidation peak at 0.015 V corresponds to that at 0.02 V for 0.05 M. For 0.01 M ketone concentration and the absence of 4-*tert*-butylcyclohexanone **1a**, no differences in the CV are observed, suggesting that the observed reaction is independent of ketone. As only H^+ pass from the anode through the membrane of the PEM cell, HER and HOR are assumed to take place on the Rh catalyst under these conditions.[16]

Fig. 6 shows a comparison of a CV from literature of the HER on Rh/Au in 0.1 M $HClO_4$ in water at 50 mV s^{-1} (Fig. 6A)[46], and the here presented CVs in cyclohexane at 10 mV s^{-1} for 0 M ketone concentration (Fig. 6B), and 1 M ketone concentration (Fig. 6C). The CV on Rh in aqueous electrolyte shows two distinct redox peaks at 0.071 mV and -0.01 V vs. RHE for the cathodic scan and two at 0.005 V and 0.151 V for the reverse scan. The peaks correspond to the HER/HOR on the Rh catalyst sites. They show comparability to the peaks observed for the HER/HOR on Pt and can be attributed to adsorbates on different crystalline structures, suggesting that multiple active sites are involved.[47]

Three peaks corresponding to these HER/HOR peaks are found in the CV in our organic PEM cell in the absence of 4-*tert*-butylcyclohexanone **1a** (Fig. 6B). In contrast, for a ketone concentration of 1 M, the redox peaks of the HER/HOR clearly vanish (Fig. 6C), indicating strong competition for active sites

between the ketone and hydrogen-related adsorbates. Such suppression of hydrogen adsorption/desorption features is commonly referred to as hydrogen underpotential deposition (H_{upd}) attributed to competitive adsorption and hydrogen site blocking on the catalyst surface, as demonstrated for organic molecules on noble metals in aqueous systems.[48]

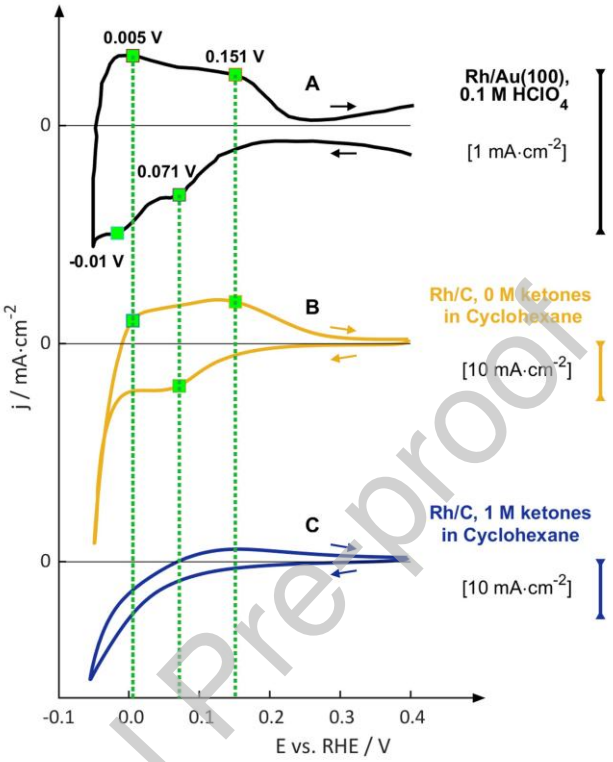

Fig. 6. Comparison of the CV on Rh: A) HER/HOR on Rh/Au in 0.1 M aqueous HClO4 at a scan rate of 50 mV s^{-1} (Reproduced from Arbib et al.[46] with permission from Journal of Electroanalytical Chemistry, 2001, ©Elsevier), B) iR-corrected CVs on Rh/C in cyclohexane at 10 mV s^{-1} for 0 M ketone concentration, and C) for 1 M. Dashed lines highlight characteristic features. For comparability, the magnitudes of the current densities are given on the right.

For very low 4-*tert*-butylcyclohexanone **1a** concentrations (0 M, 0.01 M), the HER/HOR predominates, whereas already for ketone concentrations of 0.05 M, the ketone seems to be occupying the catalyst surface partially, leaving fewer sites for protons or HER/HOR intermediates to adsorb and, hence, reduces the HER. These findings lead to the conclusion that the ketone must adsorb to the Rh surface and block sites, so that less H^+ is adsorbed by electrochemical reduction. Therefore, we can exclude the proposed mechanism ERM1, which does not consider any adsorption of ketone at the catalyst sites.

Furthermore, our investigations highlight the significance of maintaining high ketone concentrations during the electrosynthesis to suppress the competing HER and loss of Faraday efficiency.

3.2. Identification of the Reaction Mechanism

Solely by experimental analysis, it is not feasible to distinguish the LHM and ERM2 mechanisms, which both involve ketone adsorption and proton reduction at the active site: in the ERM2, adsorbed ketones react with protons, whereas in the LHM, they react with adsorbed hydrogen atoms. This section delves into the comparative analysis of the proposed mechanisms through model-based analysis. We apply the introduced dynamic kinetic model and identify for each mechanism a parameter set which best reproduces experimental CVs. A broader evaluation of simulation outputs ensures a consistent assessment of their feasibility, reaction kinetics, surface coverages, and rate-determining steps.

Table S8 (SI Section S3.1) holds the estimated kinetic parameters identified by experimental parametrization: rate constants (LHM: $k_{ket,ads}$, $k_{ket,des}$, $k_{H+,red}$, $k_{-H+,red}$, $k_{alc,form}$, $k_{-alc,form}$, $k_{alc,des}$, $k_{alc,ads}$, $k_{H_2,form}$, and for ERM2 additionally: $k_{rad,form}$, $k_{-rad,form}$), charge transfer coefficients (LHM: $\alpha_{H+,red}$, and for ERM2 additionally: $\alpha_{rad,form}$ and $\alpha_{alc,form}$), and the areal concentration of active sites Γ. The simulation results with the given parameter sets match the experimental data well with an RMSE value of 0.50 mA cm^{-2} (LHM) and 0.49 mA cm^{-2} (ERM2). The kinetic parameters of LHM and ERM2 reveal clear differences in reaction behavior. In LHM, many reactions, such as ketone adsorption ($k_{ket,ads}$ = 2.42×10^{-6} mol·s^{-1}, $k_{ket,des}$ = 2.93×10^{-6} mol· s^{-1}), show nearly equal forward and reverse rate constants, indicating quasi-reversible kinetics. ERM2, on the other hand, includes more asymmetric reactions. Notably, radical formation ($k_{rad,form}$ = 1.77×10^{-7} mol·s^{-1}, $k_{-rad,form}$ = 4.95×10^{-11} mol·s^{-1}) is highly irreversible. ERM2 also provides more charge transfer coefficients (α), suggesting a more detailed modeling of electron transfer steps. Those differences imply that ERM2 reflects more directional kinetics, whereas LHM appears more balanced. In both models, alcohol desorption shows a low k_+/k_- ratio, indicating sluggish kinetics. The observations reflect mechanistic differences between the LHM and ERM2 models, but are not indicative to determine which of the models more accurately describes the experimental behavior. In the following,

simulated CVs based on the parameter sets for LHM and ERM2 are compared with experimental data under various scan rates and ketone concentrations to further evaluate the performance of both models. Fig. 7A-F compares simulated and experimental CVs (3rd cycle) for 1 M 4-*tert*-butylcyclohexanone **1a** at various scan rates. For 10 mV s^{-1}, the experimental CVs are reproduced very well for the LHM (Fig. 7A) and ERM2 (Fig. 7D), as supported by the very low RMSE values. The CV simulations for LHM deviate slightly from the experiment, showing a delayed reaction onset in the negative going scan, while fitting well for the reverse scan. In contrast, the simulation for ERM2 fits well in the negative going scan but overestimates the oxidative current density in the reverse scan. For lower scan rates, the accuracy of the fit for the LHM simulation becomes better, especially regarding the onset, and the experiments can be well reproduced (Fig. 7B and C).

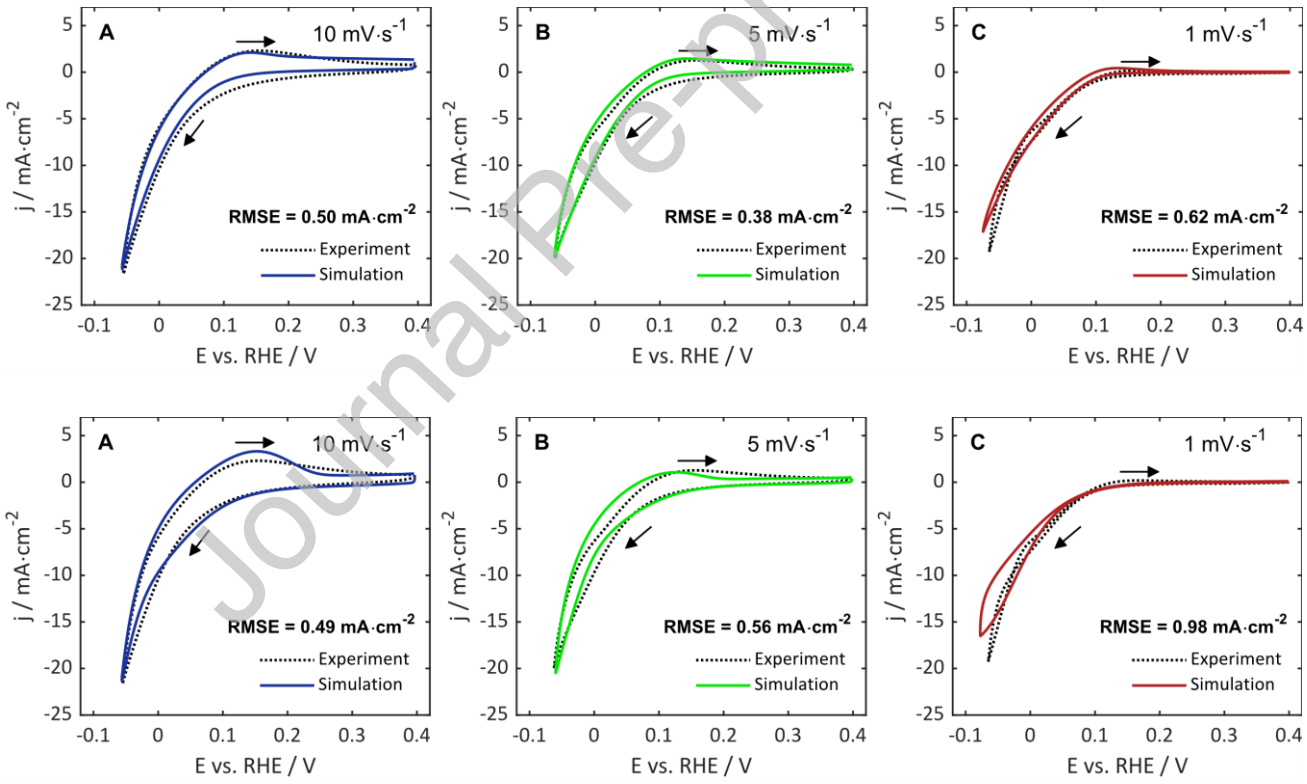

Fig. 7. Comparison of experimental (dashed) and simulated iR-corrected CVs for a variation of the scan rate (10, 5, and 1 mV s^{-1}) and a ketone concentration of 1 M for the Langmuir-Hinshelwood (LHM) kinetics (A-C) and the Eley-Rideal (ERM2) kinetics (D-F), respectively. The RMSE of each simulation is given in the graphs.

The simulations for the ERM2, on the other hand, show a shift towards more negative potential and substantially more hysteresis than in the experiments, leading to a significantly higher deviation from the experimental data than the LHM; the corresponding RMSE values in Fig. 7A-F further support these observations.

Overall, the simulations show that both models can describe trends in current densities and the convergence of the anodic and cathodic CV curves with decreasing scan rates, thus reproducing the experiments. However, the LHM simulations match the experiments better, so this mechanism appears to be the most plausible.

To prove this hypothesis, we additionally compared simulations for LHM and ERM2 and experiments for varying ketone concentrations (0.05 M, 0.01 M, and no ketone, Fig. 8A-F). It should be noted that notable deviations between experiment and simulation for HER/HOR must be expected as both mechanisms contain only a single HER and HOR step and no proton reduction on different facets, as observed experimentally in Fig. 6A and B.

It is observable in the given RMSE values and simulated CVs that the simulations show substantial deviations for all concentrations and for both mechanisms. Fig. 8A-C shows the LHM simulated CVs for the ketone concentrations 0.05 M to 0 M. The minimal current density of -19 mA cm^{-2} for the simulation of 0.05 M is marginally lower than the experimental value (-17.65 mA cm^{-2}). In contrast, at 0.01 M and 0 M, the simulation underestimates the experimental current densities. Despite these deviations in magnitude, both simulation and experiment show the same trend: the reductive current increases as the ketone concentration decreases. It can be observed that neither the experimental cathodic peak (0.07 V) nor the anodic peaks (0.015 V and 0.13 V), all attributed to the HER/HOR at different facets (see Fig. 6), can be described by the LHM simulation. Instead, similar to the high concentration simulations, only one peak in the anodic scan can be observed here, which is located at 0.12 V, 0.09 V, and 0.09 V for the different concentrations in Fig. 8A-C, respectively.

The simulation results for ERM2 show strong deviations from the experimental data, which become more pronounced at lower ketone concentrations (Fig. 8D–F).

Compared to the LHM simulations, the simulated anodic current density is overestimated for all concentrations.

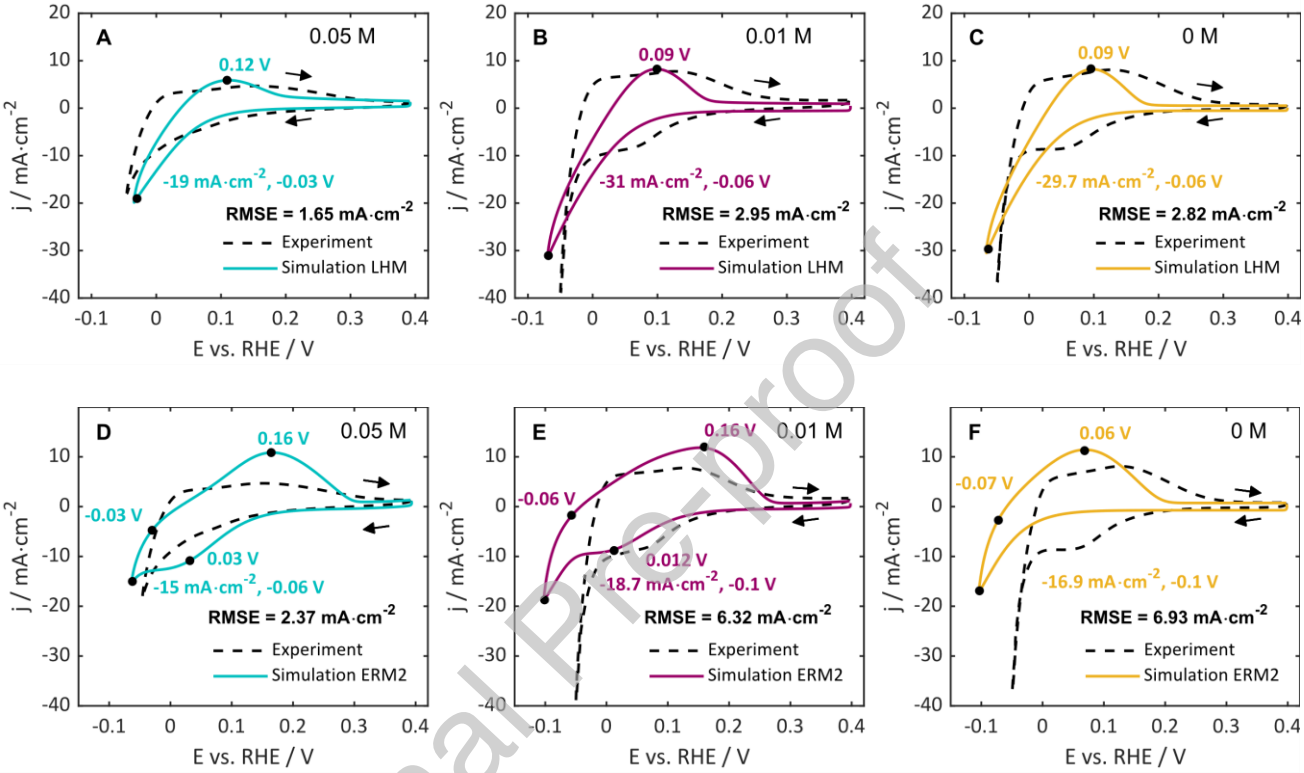

Fig. 8. Comparison of experimental (dashed) and simulated iR-corrected CVs at 10 mV s-1 for concentration variation of 4-tert-butylcyclohexanone 1a (0.05 M, 0.01 M, and 0 M) for the Langmuir-Hinshelwood (LHM) kinetics (A-C) and Eley-Rideal (ERM2) kinetics (D-F), respectively. The RMSE of each simulation is given in the graphs.

Furthermore, for 0.01 M and 0 M, the CVs have significantly lower absolute cathodic current densities than experimentally observed, and these current densities occur at significantly more negative potentials (Fig. 8E–F). Regarding peak positions, further deviations are observed: the simulated CV at 0.05 M ketone concentration (Fig. 8D) shows a cathodic peak at 0.03 V that is not present in the experiment, and anodic peaks at -0.03 V and 0.16 V. The overall CV shape differs strongly from the experimental curve. The simulation of 0.01 M follows the same trend (Fig. 8E). At 0 M, the cathodic peak is no longer visible

in the simulation (Fig. 8F), which contradicts the corresponding experimental CV, where a distinct cathodic peak appears at low ketone concentrations. In the ERM2 simulation, the disappearance of the cathodic peak at 0 M ketone concentration suggests that this feature is primarily associated with ketone reduction processes. However, experimental data clearly show that this peak is attributed to the HER (Fig. 6A and B). This indicates that the simulated kinetics of the ERM2 do not capture the experimental behavior for lower ketone concentrations. Overall, the observed trends in the ERM2 simulations for decreasing ketone concentration do not align well with the experimentally observed trends.

A significant part of the deviations observed in the simulations for both LHM and ERM2 can be attributed to the simplified one-step HER and HOR mechanisms implemented both models. This simplification cannot reproduce the complex CV features observed in plain electrolyte, which include multiple peaks arising from energetically distinct surface facets involved in HER and HOR, as also visible in Fig. 6A and B.

To assess whether the models still capture the overall electrochemical behavior despite these deviations, we conduct an analysis on a higher level of abstraction, which lumps together the different facets. The experimental and simulative anodic and cathodic charges transferred by reaction were calculated and compared (SI, section S3.2). The experimental data reveals a concentration-dependent change in charge transferred by reaction, which increases to 333 mC cm^{-2} at 0.01 M ketone concentration compared to 0 M (300 mC cm^{-2}), and shows a stronger decrease to 223 mC cm^{-2} for 0.05 M. This suggests that at 0.01 M, both HER and ketone reduction contribute to the charge transferred by reaction, while already at a 0.05 M ketone concentration, the HER is likely suppressed due to ketone adsorption. The LHM model captures this experimental behavior, particularly the concentration-dependent changes, in which the faradaic charge increases slightly from 193 mC cm^{-2} to 217 mC cm^{-2} between 0 M and 0.01 M, then decreases more sharply to 165 mC cm^{-2} at 0.05 M, whereas ERM2 fails to replicate this behavior. This indicates that LHM more accurately models the competition between ketone reduction and HER.

Beyond the analysis of the simulated CVs, we conducted a series of complementary investigations to further assess the validity and performance of both models and parameter sets.

To assess the consistency of the simulated product selectivities for the LHM and ERM2 models, Faradaic efficiencies (FEs) obtained from quasi-steady-state simulations (scan rate: 1 mV s^{-1}) are compared with experimental data from constant current electrolysis performed in the same cell setup by Shimizu et al.[16] (SI, section S3.3). For the LHM, the simulated FEs closely match the experimental trend: a high FE at low current density (LHM: 98 %, Experiment: 94 %), a slight increase in FE at the next higher current density (LHM: 98 %, Experiment: 97 %), and a clear decline in FE at high current densities (LHM: 74 %, Experiment: 60 %) (Fig. S4). In contrast, the ERM2 model failed to reach the highest current density of 24 mA cm^{-2} and exhibited significant hysteresis in the corresponding simulated CVs, deviating from experimental behavior (Fig. S5). These results highlight the reliability of the LHM model under operating conditions and its superior ability to reproduce experimentally observed selectivity trends compared to the ERM2 model.

Finally, a local sensitivity analysis was conducted to evaluate how variations in individual kinetic parameters affect the cathodic peak current density (SI, S3.4). This provides insight into the model's responsiveness and the reliability of the estimated parameter sets. In the LHM model, the proton reduction symmetry factor showed the highest sensitivity, followed by rate constants for proton and ketone adsorption and alcohol desorption. In ERM2, the most sensitive parameters were related to radical formation. All estimated parameters show responsiveness. While the results may hint at kinetic relevance, the analysis primarily confirms that all estimated parameters meaningfully influence the model response. The overall higher sensitivity in the LHM model indicates a more robust and experimentally accessible parameter set.

Altogether, the results consistently support the LHM model as the most reliable and experimentally consistent representation of the electrochemical process. While both models capture certain aspects of the observed behavior, only the LHM model reproduces key trends across all conditions, including the interplay between ketone reduction and HER, the evolution of current densities, and FEs under operating conditions. Its ability to reflect experimental trends, combined with a robust and interpretable parameter set, highlights the LHM as the most plausible basis for describing the reduction of 4-*tert*-

butylcyclohexanone **1a** in a PEM-cell. The LHM is thus identified through combined experimental and model-based analysis as the most plausible reaction mechanism.

3.3. Kinetic limitations of the electrochemical reduction of 4-*tert*-butylcyclohexanone

In this section, we analyze the reaction rates and surface coverages predicted by simulations of the LHM during cyclic voltammetry, aiming to gain deeper understanding into the kinetic limitations of the 4-*tert*-butylcyclohexanone **1a** reduction. To exclude mass transport limitations, we evaluated the simulated concentration of ketones at the electrode surface during CV (SI S3.5). The deviation from the bulk concentration remained less than 4%, confirming that the process is controlled by reaction kinetics rather than mass transport. This is consistent with the experimental flow rate comparison (SI section S3.8).

Fig. 9A shows the evolution of individual simulated reaction rates as a function of potential for 10 mV s^{-1} and 1 M ketone concentration. During the negative-going potential scan starting at 0.4 V, the rate of ketone physisorption ($r_{ket,ads}$) continuously increases without reaching saturation even at lowest potentials, indicating that this step is not significantly limited by any reactants. Its onset is observed at 0.07 V.

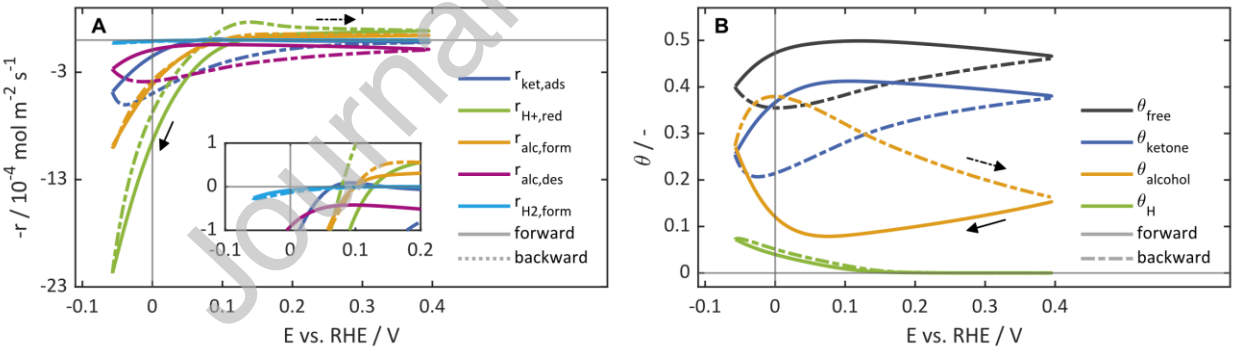

Fig. 9. Changes of the simulated reaction rates (-r) and the surface coverages θ during a CV with 10 mV s^{-1} and 1 M 4-*tert*-butylcyclohexanone **1a** concentration: A) Reaction rates for ketone adsorption ($r_{ket,ads}$), H^+ reduction ($r_{H+,red}$), 4-*tert*-butylcyclohexanol **2a** formation ($r_{alc,form}$) and desorption ($r_{alc,des}$), and H_2 formation ($r_{H_2,form}$), and B) surface coverages θ of free sites and the adsorbed species, 4-*tert*-butylcyclohexanone **1a** θ_{ketone}, 4-*tert*-butylcyclohexanol **2a** $\theta_{alcohol}$, and hydrogen θ_H. For brevity, the negative-going and positive-going scans are denoted as forward and backward, respectively.

The proton reduction rate ($r_{H+,red}$) increases exponentially, with an early onset at 0.16 V. At 0.12 V, it already exceeds the ketone adsorption rate and is approximately 4.5 times higher at the lower potential limit. The rate of alcohol formation ($r_{alc,form}$) also increases exponentially and monotonically, reaching values about twice those of ketone adsorption, but 55% lower than proton reduction. Alcohol desorption ($r_{alc,des}$) follows a similar potential-dependent trend as ketone adsorption ($r_{ket,ads}$), starting at the same potential but with a lower magnitude and a shallower slope. H_2 formation rate ($r_{H_2,form}$) remains largely constant across the potential range, with an onset at 0.03 V, as shown in the inset of Fig. 9A.

During the reverse scan, the proton reduction rate decreases, whereas ketone adsorption and alcohol desorption continue to increase briefly. This behavior reflects the relatively slow dynamics of physisorption, temporarily limiting the availability of surface sites for proton reduction. A negative proton reduction rate is observed, indicating that protons are formed from adsorbed hydrogen by oxidation, consistent with the oxidative current in the experimental CVs. This supports the interpretation that the anodic current during the reverse scan is primarily caused by the oxidation of previously adsorbed hydrogen.

Overall, it demonstrates that proton reduction occurs at high rates, emphasizing its key role in driving the surface reaction. Ketone adsorption is significantly slower, suggesting a kinetic bottleneck. Alcohol formation proceeds faster than ketone adsorption but remains significantly slower than proton reduction.

Alcohol desorption is also sluggish, highlighting its limiting role in regenerating free sites. The H_2 formation rate is the lowest among all considered processes, which should be attributed to the high ketone concentration and the rapid consumption of adsorbed hydrogen in the formation of alcohol. This observation explains the high faradaic efficiencies at high ketone concentrations and the suppression of HER, despite the rapid availability of adsorbed hydrogen.

The simulated surface coverages were analyzed to further elucidate the kinetics and associated limitations. Fig. 9B shows the changes of free surface sites and coverages of adsorbed ketone, alcohol, and hydrogen as a function of electrode potential.

At 0.4 V, 46.9 % of the Rh surface sites are free, while ketone alcohol, and hydrogen cover 38,2%, 14.9 %, and 0% of the surface, respectively. The fraction of free sites increases to 50 % at 0.1 V, then decreases to 36 % at 0 V, and then returns to the initial state at 0.4 V. The ketone coverage follows a similar trend, reaching a plateau at 21 % near 0.02 V. Alcohol coverage initially drops to 7% at 0.06 V, then rises to 36.8% at 0 V. Hydrogen coverage increases from 0.16 V to -0.05 V, reaching 7%, and then declines. The observed hysteresis in ketone adsorption and alcohol desorption reflects slow physisorption dynamics. Importantly, the free surface sites never limit, suggesting that active site availability does not constrain the reaction. The delayed increase in coverage during the positive going scan results from slow alcohol desorption and ketone adsorption, both lagging behind the changing potential and are influenced by the preceding CV cycle.

The high ketone concentration (1 M) and the high number of free sites ensure sufficient surface coverage at all potentials during the CV. The steep increase in alcohol coverage corresponds with the rapid alcohol formation ($r_{alc,form}$) and slow desorption ($r_{alc,des}$) rates, as evidenced by the steep increase in coverage below 0.06 V and the slow decline from 0.4 V to 0.06 V, as well as above 0 V. The fast proton reduction rate and the corresponding coverage of adsorbed hydrogen indicate a fast conversion to alcohol. This explains the low coverage of adsorbed hydrogen despite its high reaction rate, originating in the dominance of ketone adsorption and alcohol formation over the HER at high ketone concentrations.

To further understand how these processes behave under practical operating conditions, we additionally analyze the quasi-steady-state regime, as it occurs under potentiostatic or galvanostatic operation in an electrolyzer (SI S3.3). At a scan rate of 0.1 mV s^{-1}, which is close to steady state, the simulation shows no hysteresis (Fig. S4), indicating that the process approaches steady-state conditions during the slow CV. This allows exploration of how surface kinetics and concentration effects shape the faradaic efficiency under constant-current operation. Fig. 10A shows the evolution of reaction rates and the faradaic efficiencies under these conditions; the rates for ketone adsorption, alcohol formation, and alcohol desorption become synchronized and follow the same potential dependence, while proton reduction remains fast and exponential. The rates of ketone adsorption, alcohol formation, and alcohol desorption

each reach a distinct maximum at approximately -0.1 V, after which they begin to decline as the potential becomes more negative.

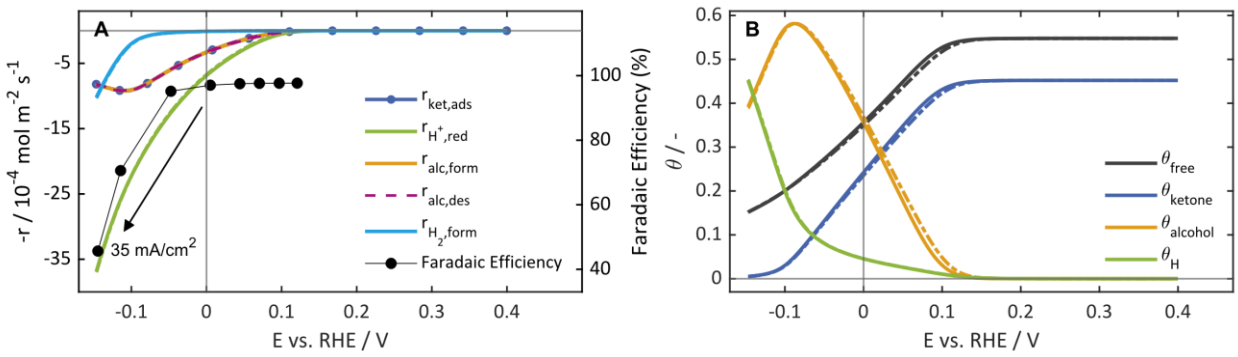

Fig. 10. Changes of the simulated reaction rates (−r), Faradaic efficiencies (FEs), and surface coverages q during a CV at 0.1 mV s^{-1} with 1 M 4-*tert*-butylcyclohexanone (**1a**) and a minimum applied potential of −0.24 V: A) Reaction rates for ketone adsorption ($r_{ket,ads}$), H^+ reduction ($r_{H+,red}$), 4-*tert*-butylcyclohexanol **2a** formation ($r_{alc,form}$) and desorption ($r_{alc,des}$), and H_2 formation ($r_{H_2,form}$). Different line styles are used for $r_{ket,ads}$, $r_{alc,form}$, and $r_{alc,des}$, which coincide over the entire potential range. In addition, the FEs of the competing reactions are shown for 0.1, 0.5, 1.5, 3, 6, 12, 25, and 35 mA cm^{-2}. Reaction rates are plotted on the left y-axis, while FEs are shown on the right y-axis. B) surface coverages θ of free sites and the adsorbed species, 4-*tert*-butylcyclohexanone **1a** θ_{ketone}, 4-*tert*-butylcyclohexanol **2a** $\theta_{alcohol}$, and hydrogen θ_H.

This behavior indicates that these processes become less favorable, leading to a significant decrease in faradaic efficiency under strongly reducing conditions, as seen in Fig. 10A. In contrast, the proton reduction rate continues to increase exponentially and reaches a value approximately four times higher than the maximum of $r_{ket,ads}$, $r_{alc,form}$, and $r_{alc,des}$, reinforcing the growing influence of hydrogen-related processes in this regime. Notably, the H_2 formation rate continues to increase exponentially and eventually dominates, resulting in a drastically lower faradaic efficiency at high current densities.

The corresponding surface coverages (Fig. 10B) reflect this shift in reactivity. The alcohol coverage initially increases to a maximum of 58.1 % at -0.1 V vs. RHE, then decreases to 39 % at the most negative potential, consistent with declining alcohol formation and desorption rates. In parallel, adsorbed hydrogen steadily accumulates, reaching 45.4 %, while the fraction of free surface sites decreases to 15.1 %. Ketone

coverage drops sharply and approaches 0.5 %, indicating that ketone adsorption becomes strongly suppressed at high overpotentials due to competitive site occupation by hydrogen.

Overall, these results demonstrate that ketone reduction dominates only within an optimal potential window, whereas HER becomes increasingly competitive at higher overpotentials, leading to reduced selectivity.

Together, these findings identify the main kinetic limitations as slow alcohol desorption and the decreasing ketone adsorption at high overpotentials. These processes control surface coverage and selectivity, ultimately defining the FE under both dynamic and steady-state conditions. Notably, these kinetic observations are further supported by thermodynamic analysis: the Gibbs free energy profile of the alcohol desorption step (Fig. S11A) reveals a positive ΔG, indicating that alcohol desorption is thermodynamically unfavorable, and ketone adsorption is slightly endergonic (SI section 3.7). Although slightly endergonic, ketone adsorption remains feasible because the adsorbed species are subsequently consumed in alcohol formation.

The kinetic, steady-state, and thermodynamic analyzes show that no single step strictly limits the overall reaction rate. Instead, both ketone adsorption and alcohol desorption are slow and jointly constrain turnover. While ketone adsorption is sustained by high concentration and sufficient surface availability, alcohol desorption is significantly slower and delays site regeneration. This kinetic imbalance becomes critical at more negative potentials, where HER starts to compete as alcohol-related rates decline. Improving ketone adsorption and alcohol desorption is therefore essential to maintain high faradaic efficiencies at higher current densities, and could reduce overpotentials and increase energy efficiency.

3.4. Simulation-driven optimization of electrochemical performance at high current densities

The developed kinetic model allows systematically investigating a wide range of operating parameters, including current density, enabling knowledge-driven optimization of productivity and efficiency. Simulations under steady-state conditions provide predictive guidance for experimental design and process improvement. The experimentally observed decrease in Faradaic efficiency from 93 % to 60 %

when increasing the current density from 12 mA cm^{-2} to 24 mA cm^{-2},[16] motivated a reassessment of operating conditions.

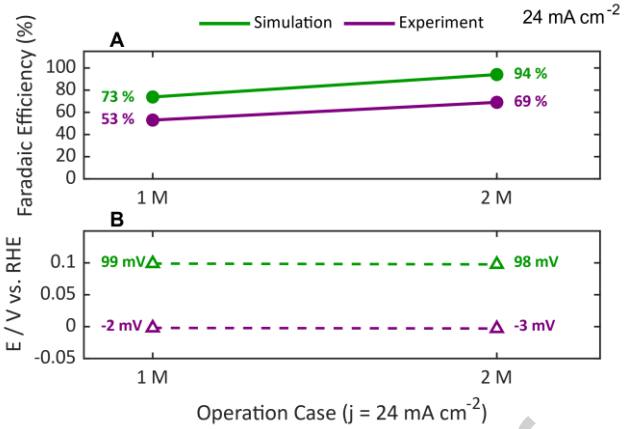

Fig. 11. Simulated and experimental Faradaic efficiencies (FE) (A) and cathode potentials (E) (B) at j = 24 mA·cm^{-2} for performance measures at 1 M and 2 M 4-*tert*-butylcyclohexanone **1a**.

Based on the preceding kinetic analysis, optimization efforts focused on mitigating the identified limitations: alcohol desorption, active site accessibility, and ketone adsorption required to displace hydrogen intermediates. As a practical first step, the ketone concentration was increased, as this directly enhances competitive adsorption and is easy to implement experimentally. Fig. 11A and B compare experimental Faradaic efficiencies and cathode potentials from constant-current electrolysis at 24 mA cm^{-2} with the corresponding simulation for the previously investigated 1 M case, and for an increased ketone concentration of 2 M. Experiment and simulation show the same trend: doubling the ketone concentration improves FE by 16-20 %. GC analysis furthermore confirms that the *cis*-selectivity remains high with 91%. Although the model slightly overestimates the effect, the excellent agreement in trend demonstrates its predictive capability. Increasing ketone concentration thus proves to be an effective optimization strategy. Importantly, the model also correctly predicts negligible changes in potential upon increasing ketone concentration, which makes it feasible for model-assisted energy optimization. However, a systematic potential offset of approximately 100 mV is observed between experiment and simulation at

higher current densities. This offset is likely caused by the simplified iR-correction applied in the model and is discussed in detail in the SI in sections S3.3 and S3.8.

Moreover, the model was used to investigate the effects of increasing catalyst loading and changes in surface roughness (SI section S3.8). Experiment and simulation show that increasing catalyst loading does not improve performance, because the associated changes in diffusion-layer thickness counteract the increase in active sites. Further simulations indicate that increasing surface roughness would provide a clear performance benefit by enlarging the accessible active surface without inducing unfavorable mass transport effects. Although the experimental realization of such geometric modifications is challenging in the investigated cell design, the model predictions underscore the potential of approaches to enhance the electrochemically active surface area. Altogether, the study demonstrates that the kinetic model translates mechanistic insights into practical optimization measures. The qualitative agreement with experiment supports its predictive capability for identifying improvements in operating conditions and overall process performance.

4. Conclusions

This study establishes a robust framework for understanding and optimizing the electrochemical reduction of 4-*tert*-butylcyclohexanone **1a** to 4-*tert*-butylcyclohexanol **2a** in a PEM cell. The Langmuir-Hinshelwood mechanism (LHM), where adsorbed hydrogen reacts with adsorbed ketone, was identified as the most reliable and experimentally consistent representation of the hydrogenation. The corresponding model accurately reproduces the evolution of current densities, the decreasing hysteresis of the CV with decreasing scan rate, and the concentration dependence of the CVs. Simulated Faradaic charges align well with experimental data under dynamic conditions, and quasi-steady-state simulations successfully reproduce the Faradaic efficiencies observed during constant current electrolysis. Sensitivity analysis confirms the robustness of the LHM parameter set. While the Eley-Rideal mechanism ERM2 captures some qualitative trends, only the LHM consistently reproduces all key experimental observations, particularly the interplay between ketone reduction and hydrogen evolution.

Kinetic analysis highlights two critical process limitations: slow ketone adsorption and sluggish alcohol desorption. While ketone adsorption influences the selectivity, alcohol desorption delays surface site regeneration, particularly under steady-state conditions. Hydrogen evolution becomes competitive at low ketone concentrations but is suppressed at higher concentrations due to preferential surface occupation by ketone-derived intermediates. This aligns with the CV observations, where HER dominates only in the absence or at very low concentrations of ketone, while the ketone-related mechanism prevails at concentrations as low as 0.05 M. The kinetic insights confirm that anodic current arises from reversible hydrogen oxidation and that overall turnover is governed by the interplay of alcohol desorption, ketone adsorption, and hydrogen dynamics. These findings provide a framework for interpreting experimental features and guiding optimization.

Two key factors are identified as prerequisite to achieve high selectivity and efficiency in electrochemical ketone reduction on Rh/C: a sorption-controlled reaction mechanism and the distinct electrochemical properties of Rh. The requirement for adsorbed ketone and adsorbed hydrogen excludes outer-sphere pathways and ensures that only specific surface-bound intermediates contribute to product formation.

Despite efficient mass transport, overall turnover remains low compared to typical PEM electrolysis systems (e.g., 36 vs. >1000 mA cm^{-2}). Our investigation reveals that this limitation arises from surface kinetics, particularly the sluggish physisorption of ketone and the slow desorption of alcohol. These processes restrict the effective utilization of active sites and limit higher achievable current densities at similar faradaic efficiencies and *cis*-selectivity of the desired product.

Simulations under quasi-steady-state conditions suggest that increasing the ketone concentration improves ketone coverage on the catalyst surface and reduces the number of adsorbed hydrogen atoms, thereby increasing the Faraday efficiency. Experiments validated the predictions. Also, our analysis suggests further potential for optimization, such as identifying other catalyst to promote alcohol desorption, and improving catalyst structure and morphology to increase the number of active sites.

Overall, this work demonstrates that dynamic kinetic modeling is a powerful method to elucidate reaction mechanisms and transport phenomena in electrosynthesis. It enables predictive process and performance optimization and supports the rational design and optimal operation of flow electrolysis cells.

Data Availability Statement

The data presented in the manuscript are openly available in the KITopen repository at DOI: 10.35097/pnmem7c42eezkx89 (not yet available).

Acknowledgments

The authors acknowledge the financial support by the BMBF – Federal Ministry for Education and Research of Germany as part of the Cluster4Future ETOS (Electrifying Technical Organic Electrosynthesis) and the projects DigiE-tos (03ZU1205NA) and Training4ETOS (03ZU1205QB). We also thank for support by the Japan Science and Technology Agency (JST) as part of the Adopting Sustainable Partnerships for Innovative Research Ecosystem (ASPIRE, Grant Number JPMJAP2528).

Author Contributions

Swantje Pauer: Writing – original draft, validation, software, methodology, investigation, formal analysis, data curation. Philipp Röse: Writing – review & editing, supervision, methodology, formal analysis, conceptualization. Yugo Shimizu and Juri Harada: designed and performed experiments. Naoki Shida: Writing – review & editing, supervision, resources, conceptualization. Mahito Atobe: Writing – review & editing, supervision, resources, conceptualization. Ulrike Krewer: Writing – review & editing, supervision, methodology, resources, conceptualization.

Appendix. Supporting Information

Download-link for the document with Supplementary Information, referred to in the main text.

The authors have cited additional references within the Supporting Information.[49–57]

References

[1] Y. Kloo, L.J. Nilsson, E. Palm, Reaching net-zero in the chemical industry—A study of roadmaps for industrial decarbonisation, Renew. Sustain. Energy Transit. 5 (2024) 100075. https://doi.org/10.1016/j.rset.2023.100075.

[2] J.L. Barton, Electrification of the chemical industry, Science 368 (2020) 1181–1182. https://doi.org/10.1126/science.abb8061.

[3] P. Röse, P. Neugebauer, S. Tamang, S.R. Waldvogel, U. Krewer, Trends and Challenges in Electrifying Technical Organic Synthesis, Chem. Ing. Tech. 97 (2025) 395–410. https://doi.org/10.1002/cite.202400155.

[4] H. Ilikti, N. Rekik, M. Thomalla, Electrocatalytic hydrogenation of alkyl-substituted phenols in aqueous solutions at a Raney nickel electrode in the presence of a non-micelle-forming cationic surfactant, J. Appl. Electrochem. 34 (2004) 127–136. https://doi.org/10.1023/B:JACH.0000009932.06652.a0.

[5] F. Yan, Y. Sang, Y. Bai, K. Wu, K. Cui, Z. Wen, F. Mai, Z. Ma, L. Yu, H. Chen, Y. Li, Guaiacol demethoxylation catalyzed by Re2O7 in ethanol, Catal. Today 355 (2020) 231–237. https://doi.org/10.1016/j.cattod.2019.07.018.

[6] P. Maity, M. Gujjar, R. Vellingiri, T. Lakshminarasimhan, A.J. DelMonte, I.S. Young, M.D. Eastgate, R. Vaidyanathan, Cerium(III) Chloride-Mediated Stereoselective Reduction of a 4-Substituted Cyclohexanone Using $NaBH_4$, Org. Process Res. Dev. 23 (2019) 2754–2757. https://doi.org/10.1021/acs.oprd.9b00458.

[7] S. Arctander, Perfume and flavor chemicals: aroma chemicals, Allured Publishing Corporation, Carol Stream, IL, 2000.

[8] D.Yu. Murzin, A.I. Allachverdiev, N.V. Kul'kova, Kinetics of the liquid-phase stereoselective hydrogenation of 4-tertbutylphenol over rhodium catalyst, in: Stud. Surf. Sci. Catal., Elsevier, 1993: pp. 243–250. https://doi.org/10.1016/S0167-2991(08)63326-1.

[9] D.Y. Murzin, S.R. Konuspaev, Hydrogenation of 4-tert-butylphenol in a three-phase cocurrent upflow reactor, Catal. Today 79–80 (2003) 229–233. https://doi.org/10.1016/S0920-5861(03)00009-9.

[10] N. Hiyoshi, C. Rode, O. Sato, H. Tetsuka, M. Shirai, Stereoselective hydrogenation of tert-butylphenols over charcoal-supported rhodium catalyst in supercritical carbon dioxide solvent, J. Catal. 252 (2007) 57–68. https://doi.org/10.1016/j.jcat.2007.08.011.

[11] B. Huang, Y. Li, C. Yang, W. Xia, Electrochemical 1,4-reduction of α,β-unsaturated ketones with methanol and ammonium chloride as hydrogen sources, Chem. Commun. 55 (2019) 6731–6734. https://doi.org/10.1039/C9CC02368B.

[12] T. Shono, I. Nishiguchi, H. Omizu, REDUCTIVE CYCLIZATION OF NONCONJUGATED ACETYLENIC KETONES TO 2- METHYLENECYCLOPENANOLS, Chem. Lett. 5 (1976) 1233–1236. https://doi.org/10.1246/cl.1976.1233.

[13] K. Sun, Z. Xu, V. Ramadoss, L. Tian, Y. Wang, Electrochemical deoxygenative reduction of ketones, Chem. Commun. 58 (2022) 11155–11158. https://doi.org/10.1039/D2CC04548F.

[14] W. Li, R. Zhang, N. Zhou, J. Lu, N. Fu, Dual transition metal electrocatalysis enables selective $C(sp^3)$–$C(sp^3)$ bond cleavage and arylation of cyclic alcohols, Chem. Commun. (2024) 10.1039.D4CC04036H. https://doi.org/10.1039/D4CC04036H.

[15] J.P. Coleman, R.J. Kobylecki, J.H.P. Utley, Stereoselective electrochemical reduction of cyclic ketones, J. Chem. Soc. Chem. Commun. (1971) 104. https://doi.org/10.1039/c29710000104.

[16] Y. Shimizu, J. Harada, A. Fukazawa, T. Suzuki, J.N. Kondo, N. Shida, M. Atobe, Diastereoselective Electrocatalytic Hydrogenation of Cyclic Ketones Using a Proton-Exchange Membrane Reactor: A Step toward the Electrification of Fine-Chemical Production, ACS Energy Lett. (2023) 1010–1017. https://doi.org/10.1021/acsenergylett.2c02573.

[17] R. Fonocho, C.L. Gardner, M. Ternan, A study of the electrochemical hydrogenation of o-xylene in a PEM hydrogenation reactor, Electrochimica Acta 75 (2012) 171–178. https://doi.org/10.1016/j.electacta.2012.04.116.

[18] A. Fukazawa, K. Takano, Y. Matsumura, K. Nagasawa, S. Mitsushima, M. Atobe, Electrocatalytic Hydrogenation of Toluene Using a Proton Exchange Membrane Reactor: Influence of Catalyst Materials on Product Selectivity, Bull. Chem. Soc. Jpn. 91 (2018) 897–899. https://doi.org/10.1246/bcsj.20180021.

[19] A. Fukazawa, Y. Shimizu, N. Shida, M. Atobe, Electrocatalytic hydrogenation of benzoic acids in a proton-exchange membrane reactor, Org. Biomol. Chem. 19 (2021) 7363–7368. https://doi.org/10.1039/D1OB01197A.

[20] M.J. Torres, P. Sánchez, A. De Lucas-Consuegra, A.R. De La Osa, Electrocatalytic hydrogenation of cinnamaldehyde in a PEM cell: The role of sodium hydroxide and platinum loading, Mol. Catal. 492 (2020) 110936. https://doi.org/10.1016/j.mcat.2020.110936.
[21] K. Takano, H. Tateno, Y. Matsumura, A. Fukazawa, T. Kashiwagi, K. Nakabayashi, K. Nagasawa, S. Mitsushima, M. Atobe, Electrocatalytic Hydrogenation of Toluene Using a Proton Exchange Membrane Reactor, Bull. Chem. Soc. Jpn. 89 (2016) 1178–1183. https://doi.org/10.1246/bcsj.20160165.
[22] S.K. Green, G.A. Tompsett, H.J. Kim, W.B. Kim, G.W. Huber, Electrocatalytic Reduction of Acetone in a Proton-Exchange-Membrane Reactor: A Model Reaction for the Electrocatalytic Reduction of Biomass, ChemSusChem 5 (2012) 2410–2420. https://doi.org/10.1002/cssc.201200416.
[23] S. Nogami, N. Shida, S. Iguchi, K. Nagasawa, H. Inoue, I. Yamanaka, S. Mitsushima, M. Atobe, Mechanistic Insights into the Electrocatalytic Hydrogenation of Alkynes on Pt–Pd Electrocatalysts in a Proton-Exchange Membrane Reactor, ACS Catal. 12 (2022) 5430–5440. https://doi.org/10.1021/acscatal.2c01594.
[24] S. Carl, K. Waldrop, P. Pintauro, L.T. Thompson, W.A. Tarpeh, Selective Hydrogenation of Furfural in a Proton Exchange Membrane Reactor Using Hybrid Pd/Pd Black on Alumina, ChemElectroChem 6 (2019) 5563–5570. https://doi.org/10.1002/celc.201901314.
[25] A. Villagra, P. Millet, An analysis of PEM water electrolysis cells operating at elevated current densities, Int. J. Hydrog. Energy 44 (2019) 9708–9717. https://doi.org/10.1016/j.ijhydene.2018.11.179.
[26] K.W. Ahmed, M.J. Jang, M.G. Park, Z. Chen, M. Fowler, Effect of Components and Operating Conditions on the Performance of PEM Electrolyzers: A Review, Electrochem 3 (2022) 581–612. https://doi.org/10.3390/electrochem3040040.
[27] I. Chorkendorff, J.W. Niemantsverdriet, Concepts of modern catalysis and kinetics, 3rd, completely rev. and enl. ed. ed., Wiley-VCH GmbH & Co. KGaA, Weinheim, 2017.
[28] M.V. Ferreira, J.M. Loureiro, Number of Actives Sites in TAME Synthesis: Mechanism and Kinetic Modeling, Ind. Eng. Chem. Res. 43 (2004) 5156–5165. https://doi.org/10.1021/ie0308801.
[29] D. Kiani, I.E. Wachs, Practical Considerations for Understanding Surface Reaction Mechanisms Involved in Heterogeneous Catalysis, ACS Catal. 14 (2024) 16770–16784. https://doi.org/10.1021/acscatal.4c05188.
[30] B.J.M. Etzold, U. Krewer, S. Thiele, A. Dreizler, E. Klemm, T. Turek, Understanding the activity transport nexus in water and CO2 electrolysis: State of the art, challenges and perspectives, Chem. Eng. J. 424 (2021) 130501. https://doi.org/10.1016/j.cej.2021.130501.
[31] J. Geppert, F. Kubannek, P. Röse, U. Krewer, Identifying the oxygen evolution mechanism by microkinetic modelling of cyclic voltammograms, Electrochimica Acta 380 (2021) 137902. https://doi.org/10.1016/j.electacta.2021.137902.
[32] A. Medrano-Banda, J. Guehl, G. Kéranguéven, A. Oshchepkov, E. Savinova, A. Bonnefont, Dual-path glucose electrooxidation reaction on Ni(OH)2/NiOOH catalysts in alkaline media, Electrochimica Acta 476 (2024) 143692. https://doi.org/10.1016/j.electacta.2023.143692.
[33] I. Dorner, P. Röse, U. Krewer, Dynamic vs. Stationary Analysis of Electrochemical Carbon Dioxide Reduction: Profound Differences in Local States, ChemElectroChem 10 (2023) e202300387. https://doi.org/10.1002/celc.202300387.
[34] N. Oppel, P. Röse, S. Heuser, M. Prokein, U.-P. Apfel, U. Krewer, Unveiling the kinetics of CO2 reduction in aprotic electrolyte: The critical role of adsorption, Electrochimica Acta 490 (2024) 144270. https://doi.org/10.1016/j.electacta.2024.144270.
[35] J. Geppert, P. Röse, S. Czioska, D. Escalera-López, A. Boubnov, E. Saraçi, S. Cherevko, J.-D. Grunwaldt, U. Krewer, Microkinetic Analysis of the Oxygen Evolution Performance at Different Stages of Iridium Oxide Degradation, J. Am. Chem. Soc. 144 (2022) 13205–13217. https://doi.org/10.1021/jacs.2c03561.
[36] J. Geppert, P. Röse, S. Pauer, U. Krewer, Microkinetic Barriers of the Oxygen Evolution on the Oxides of Iridium, Ruthenium and their Binary Mixtures, ChemElectroChem 9 (2022) e202200481. https://doi.org/10.1002/celc.202200481.
[37] O. Sorsa, J. Nieminen, P. Kauranen, T. Kallio, Stable Reference Electrode in Polymer Electrolyte Membrane Electrolyser for Three-Electrode Measurements, J. Electrochem. Soc. 166 (2019) F1326–F1336. https://doi.org/10.1149/2.0461916jes.
[38] D. Garcia-Pintos, J. Voss, A.D. Jensen, F. Studt, Hydrodeoxygenation of Phenol to Benzene and Cyclohexane on Rh(111) and Rh(211) Surfaces: Insights from Density Functional Theory, J. Phys. Chem. C 120 (2016) 18529–18537. https://doi.org/10.1021/acs.jpcc.6b02970.
[39] E. Gileadi, Electrode kinetics: for chemists, chemical engineers, and materials scientists, 1. printing, VCH, New York, NY Weinheim Cambridge, United Kingdom, 1993.

[40] J.K. Nørskov, T. Bligaard, A. Logadottir, J.R. Kitchin, J.G. Chen, S. Pandelov, U. Stimming, Trends in the Exchange Current for Hydrogen Evolution, J. Electrochem. Soc. 152 (2005) J23. https://doi.org/10.1149/1.1856988.
[41] P. Schön, U. Krewer, Revealing the complex sulfur reduction mechanism using cyclic voltammetry simulation, Electrochimica Acta 373 (2021) 137523. https://doi.org/10.1016/j.electacta.2020.137523.
[42] A.J. Bard, L.R. Faulkner, H.S. White, Electrochemical methods: fundamentals and applications, Third edition, Wiley, Hoboken, NJ, 2022.
[43] M.T. Tyn, W.F. Calus, Diffusion coefficients in dilute binary liquid mixtures, J. Chem. Eng. Data 20 (1975) 106–109. https://doi.org/10.1021/je60064a006.
[44] D.-W. Chung, M. Ebner, D.R. Ely, V. Wood, R. Edwin García, Validity of the Bruggeman relation for porous electrodes, Model. Simul. Mater. Sci. Eng. 21 (2013) 074009. https://doi.org/10.1088/0965-0393/21/7/074009.
[45] Q. Chen, Z. Niu, H. Li, K. Jiao, Y. Wang, Recent progress of gas diffusion layer in proton exchange membrane fuel cell: Two-phase flow and material properties, Int. J. Hydrog. Energy 46 (2021) 8640–8671. https://doi.org/10.1016/j.ijhydene.2020.12.076.
[46] M. Arbib, B. Zhang, V. Lazarov, D. Stoychev, A. Milchev, C. Buess-Herman, Electrochemical nucleation and growth of rhodium on gold substrates, J. Electroanal. Chem. 510 (2001) 67–77. https://doi.org/10.1016/S0022-0728(01)00545-9.
[47] N. Farfour, M. El Mahi Chbihi, D. Takky, K. Eddahaoui, S. Benmokhtar, Catalytic oxidation of methanol on Pt/X (X = CaTP, NaTP) electrodes in sulfuric acid solution, Mediterr. J. Chem. 2 (2013) 595–606. https://doi.org/10.13171/mjc.2.4.2013.12.10.23.
[48] N. Singh, U. Sanyal, J.L. Fulton, O.Y. Gutiérrez, J.A. Lercher, C.T. Campbell, Quantifying Adsorption of Organic Molecules on Platinum in Aqueous Phase by Hydrogen Site Blocking and in Situ X-ray Absorption Spectroscopy, ACS Catal. 9 (2019) 6869–6881. https://doi.org/10.1021/acscatal.9b01415.
[49] O. Diaz-Morales, D. Ferrus-Suspedra, M.T.M. Koper, The importance of nickel oxyhydroxide deprotonation on its activity towards electrochemical water oxidation, Chem. Sci. 7 (2016) 2639–2645. https://doi.org/10.1039/C5SC04486C.
[50] M.L. Campbell, Cyclohexane, in: Wiley-VCH Verlag GmbH & Co. KGaA (Ed.), Ullmanns Encycl. Ind. Chem., Wiley-VCH Verlag GmbH & Co. KGaA, Weinheim, Germany, 2011: p. a08_209.pub2. https://doi.org/10.1002/14356007.a08_209.pub2.
[51] G.L. Bas, The Molecular Volumes of Liquid Chemical Compounds, from the Point of View of Kopp, Longmans, Green, 1915. https://books.google.de/books?id=6FUuAQAAIAAJ.
[52] O.R. Quayle, The Parachors of Organic Compounds. An Interpretation and Catalogue, Chem. Rev. 53 (1953) 439–589. https://doi.org/10.1021/cr60166a003.
[53] U. Krewer, H.-K. Yoon, H.-T. Kim, Basic model for membrane electrode assembly design for direct methanol fuel cells, J. Power Sources 175 (2008) 760–772. https://doi.org/10.1016/j.jpowsour.2007.09.115.
[54] Y.-C. Chen, C. Karageorgiou, J. Eller, T.J. Schmidt, F.N. Büchi, Determination of the porosity and its heterogeneity of fuel cell microporous layers by X-ray tomographic microscopy, J. Power Sources 539 (2022) 231612. https://doi.org/10.1016/j.jpowsour.2022.231612.
[55] T. Jaster, A. Gawel, D. Siegmund, J. Holzmann, H. Lohmann, E. Klemm, U.-P. Apfel, Electrochemical CO2 reduction toward multicarbon alcohols - The microscopic world of catalysts & process conditions, iScience 25 (2022) 104010. https://doi.org/10.1016/j.isci.2022.104010.
[56] K. Jiang, Y. Huang, G. Zeng, F.M. Toma, W.A. Goddard, A.T. Bell, Effects of Surface Roughness on the Electrochemical Reduction of CO_2 over Cu, ACS Energy Lett. 5 (2020) 1206–1214. https://doi.org/10.1021/acsenergylett.0c00482.
[57] L. Yu, S. Sun, H. Li, Z.J. Xu, Effects of catalyst mass loading on electrocatalytic activity: An example of oxygen evolution reaction, Fundam. Res. 1 (2021) 448–452. https://doi.org/10.1016/j.fmre.2021.06.006.

Graphical abstract

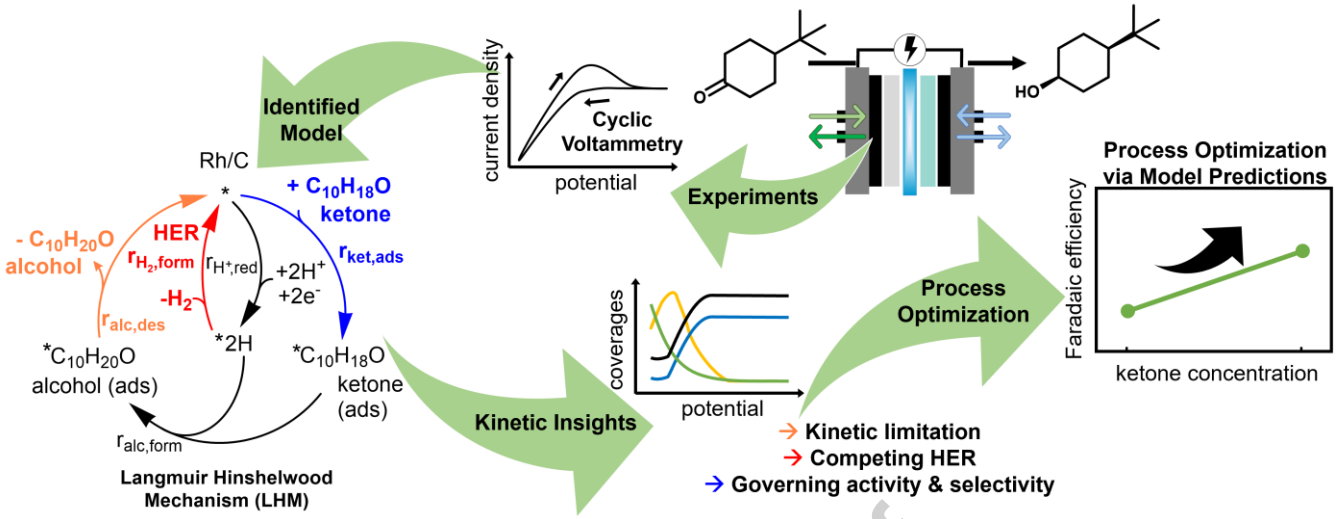

Declaration of interests

☒ The authors declare that they have no known competing financial interests or personal relationships that could have appeared to influence the work reported in this paper.

☐ The authors declare the following financial interests/personal relationships which may be considered as potential competing interests: